Electrically Driven Rotation and Nonreciprocal Motion of Microparticles in Nematic Liquid Crystals

Nikita V. Solodkov, Antariksh Saxena, and J. Cliff Jones*

Dispersion of microparticles in nematic liquid crystals offers a novel means for controlling both their orientation and position through the combination of topology and external stimuli. Here, cuboidal and triangular prism shaped microparticles in parallel plate capacitor cells filled with a nematic liquid crystal are studied. Experimental observations are compared with numerical simulations to show that the optimal orientation of the particles is determined by their aspect rations, the relative separation gap of their containers and the applied voltage. It is observed that in systems that allow unrestricted particle rotation, the long axes of the particles are able to fully align themselves with the external electric field. However, when particle rotation is geometrically restricted, it is found that increasing the voltage past a critical value causes the short axis of the particle to realign with the electric field due to anchoring breaking. It is shown that symmetry of the particles then plays a key role in their dynamics following the removal of the electric field, allowing the triangular prisms to travel perpendicular to the applied electric field, whereas only rotation is possible for the cuboidal particles.

1. Introduction

Deliberate manipulation of microparticles and nanoparticles offers the material scientist and application engineer an invaluable tool for controlling functional materials.[1] Whether in the field of biology, photonics or microrobotics, the ability to move and orient solid components within a liquid matrix has enormous potential for a variety of applications.[2–6] A familiar and commercially successful example of this is the electrophoretic display that is used for e-paper, in which microcapsules containing a dispersion of bicolored nanoparticles are suspended in a polymer matrix.[7] The nanoparticles are arranged with different zeta-potentials to allow electric field manipulation of their position within each droplet, thereby allowing an electrically controllable "ink on paper" appearance. Efforts to

induce threshold behavior in such droplets through the addition of a nematic liquid crystal (NLC) matrix have been proposed,[8] though not realized experimentally. Other possibilities that also yet remain visions of their inventors include the self-assembly of colloidal and emulsion systems with potential applications for optical computers[9–11] and biological sensors.[12,13] Meeting such potential, however, will require particles and media that are significantly more functional than the simple system used for e-paper. One of the more promising approaches is that of nematic liquid crystal dispersions. Recently, there has been a wealth of activity in using nematic liquid crystals as hosts for particulate dispersions due to their optical and electrically controllable and anisotropic nature.[12–23] NLCs are ordered fluids, in which the constituent anisotropic molecules exhibit long range orientational order.[24] In such a system, the molecules have no positional order but share a common pointing direction, described by headless unit pseudovector **n**, called the director. In the simplest form, NLCs are described by (uniaxial) cylindrical symmetry, which makes **n**, along with all of its associated physical observable properties, indistinguishable from −**n**.[25–27] To describe these properties in a given domain, it is common to use the nematic order tensor

$$Q_{ij} = Q\left(n_i n_j - \frac{\delta_{ij}}{3}\right) \tag{1}$$

where Q is the scalar order parameter and δ_{ij} is the Kronecker delta, with $\{i, j \in \mathbb{N} \,|\, 1 \leq i, j \leq 3\}$.[24] Similar to normal mathematical vector fields, director fields are strongly influenced by boundary conditions (BCs) and topological rules.[26–30] For example, the director around a sphere with tangential boundary conditions must have a set of singularities on its surface (cf. flow around a sphere in fluid mechanics).[31] These singularities are called topological defects and are described by a property known as a topological charge. This is a measure of the number of turns made by **n** in a closed loop or surface around an isolated singularity and remains invariant in a closed system with fixed boundary conditions.[27,31,32] Since nematics are comprised of real molecules, the defects in the director field manifest themselves as small isolated regions (typically of the order of tens of nm) with localized melting to the isotropic phase, where $Q = 0$, when assuming that any induced biaxiality[33] is negligible.

Dr. N. V. Solodkov, Dr. A. Saxena, Prof. J. C. Jones
School of Physics and Astronomy
University of Leeds
Leeds LS2 9JT, UK
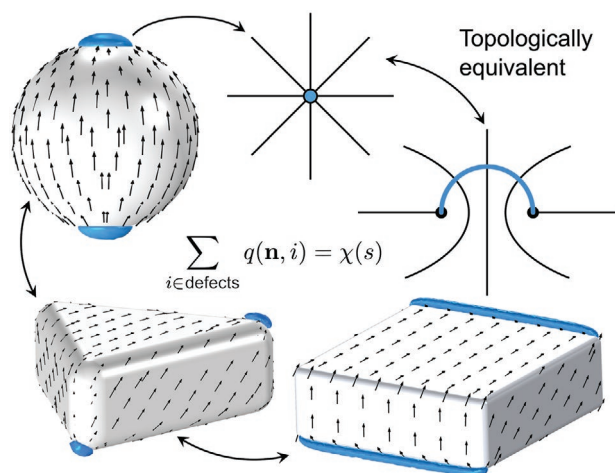E-mail: J.C.Jones@leeds.ac.uk

Figure 1. Nematic director field and topological defects on the surfaces of particles. Illustration showing the topological equivalence of the nematic director fields (black arrows and streamlines) on the surfaces of different 3D geometric shapes with tangential boundary conditions and the corresponding possibilities of the resulting topological defects (blue volumes). This results in two +1 topological defects that are situated as far away as possible from each other to minimize elastic distortion. Each +1 defect is topologically equivalent to two +1/2 defects, which are also observed experimentally. The sum of all individual topological charges, $q(n, i)$ for $i \in$ defects, on a given surface, s, must equal to its Euler characteristic, $\chi(s)$, which is equal to 2 for a 2-sphere and other topologically equivalent shapes. Note, the defects are not shown to scale for the micro-particles used in this work but are shown for illustrative purposes only.

Additionally, due to the head-tail symmetry of the director, topological defects with half integer charges are also possible. To minimize their contribution to the free energy of the system, the defects have a natural tendency to relax into regions of space that best match their local director curvatures. An early commercial adopter of this characteristic is the Zenithal Bistable Display,[34,35] in which the process of creation and annihilation of NLC defects at structured surfaces is used as a means of switching between two stable configurations of the director. **Figure 1** illustrates the topological equivalence of spheres, cuboids, and triangular prisms, as well as combinations of topological charges on the curved surfaces of 3D objects, such as colloidal and microparticle inclusions. In these examples, degenerate tangential BCs of the local surface director are assumed.

NLC dispersions are highly susceptible to topology and boundary conditions that can produce long range gradients in the director fields and promote the self-assembly of structures with varying complexity, ranging from linear chains to crystal-like structures[15,16,36,37] and fractals[23,38] with a variety of possible applications. For example, recent studies have shown that clusters of nanoparticles can be used in NLC hosts to create fast switching, voltage, and temperature controlled, light scattering transparency windows.[39,40] Furthermore, geometrical properties of the dispersions,[14,19,37,41,42] as well as that of the bounding domains,[23,43] can have a strong influence on their configurations in NLCs.

In this work, we demonstrate the importance of the geometry of the dispersed particles on their behavior in NLC hosts. The systems are studied both numerically and experimentally to distinguish the key factors that influence the orientation of the particles. A similar set of systems has been investigated in

recent studies by Lapointe et al.[14] and Yuan et al.[22] The first study investigates in-plane and out-of-plane electrical switching properties of torus-like cuboidal microparticle platelets, while the second, the spinning of particles mediated by polarizing light. By contrast, our work focuses on determining the optimal configurations of microparticle platelets as a function of their aspect ratios and containment. Following this, we induce rotation and nonreciprocal motion of the dispersed particles in a direction that is perpendicular to that of the applied electric field and determined by the symmetry of the microparticles, with the aim of providing controlled motion for potential applications.

2. Results and Discussion

Cuboidal and triangular prism shaped particles were created from SU-8 photoresist using a 2D direct write laser photolithography process.[44] Particles with length $L = 15$ μm, thickness $T = 5$ μm, and width $W = 15$ μm (see **Figure 2**A) were dispersed into the commercial NLC mixture MLC-6204-000 (Merck Chemicals Ltd.), which has a highly positive dielectric anisotropy of +29.3 at 25 °C and 1 to 100 kHz. The system was then studied under various conditions inside parallel plate capacitor glass cells, with an inner separation gap d and normal BCs at the surfaces (induced by prior coating with the commercial homeotropic polyimide alignment layer SE1211 from Nissan Chemicals), and observed using transmission polarized light microscopy. The nature of the interaction between SU-8 and the NLC led to degenerate tangential BCs of the director field at the particles' surfaces. Following this, we used the phenomenological Landau–de Gennes representation of the free energy to model the nematic director and the nematic order tensor fields around the particles using the finite element analysis approach.[24,27,45–47]

To minimize the free energy of the system, the liquid crystal director field must construct itself in a way that both satisfies the boundary conditions on the contacting surfaces and minimizes the elastic distortion throughout the bulk. From this, for example, we can expect that the cuboid will assume an equilibrium at an angle to the plane of the cell such that there are defects on the top and bottom corners of the particle (that is, the corners closest to the bounding surfaces). By considering the symmetry of the particles, their orientation can usually be reduced to a single out of plane tilt angle, θ_0, in a particular vertical plane. For the case of cuboids, we assume that $T \leq L \leq W$ and that this angular orientation occurs in the L–T plane. An example of this is illustrated in Figure 2B, where the optimal orientation of a cuboid shaped particle in the L–T plane is shown. From the 2D simulations, we observe that θ_0 depends on the particle's aspect ratio, L/T, as well as the relative size of the cell gap. For systems in which the particle's 2D diagonal length, $D_{2D} = \sqrt{L^2 + T^2}$, is greater than d, θ_0 is geometrically restricted to a certain range, beyond which the particle cannot tilt further, which defines the blocked region in Figure 2C. In fact, two such regions exist: one in which the particle is able to lay in the plane of the cell, where $d \in [T, D_{2D})$ and $\theta_0 \in [0°, (\text{asin}d/D_{2D} - \text{atan}T/L)]$, and the other in which the particle can stand perpendicular to it, where $d \in [L, D_{2D})$ and $\theta_0 \in [(90° + \text{atan}L/T - \text{asin}d/D_{2D}), 90°]$, which is shown as a secondary region in Figure 2C. However, the second possibility

ADVANCED
SCIENCE NEWS
www.advancedsciencenews.com

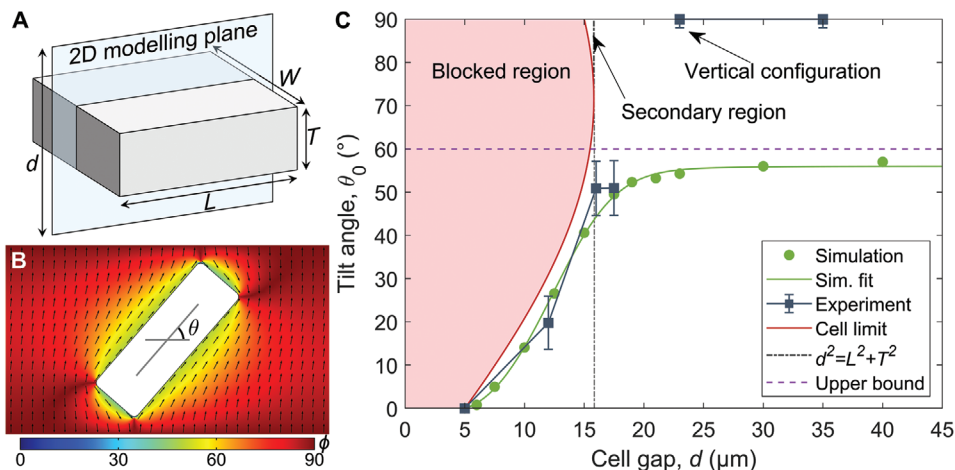NANO · MICRO
small
www.small-journal.com

Figure 2. 2D numerical simulations of a cuboid shaped particle's out of plane tilt in cells filled with MLC-6204-000 NLC. A) Schematic illustration of the 2D modeling plane for a cuboid shaped particle with length L, thickness T, and depth W inside a cell with a cell gap d. B) Optimal orientation of a particle with tangential boundary conditions ($L = 15$ µm, $T = 5$ µm) inside a nematic director field with normal boundary conditions on upper and lower surfaces of the cell ($d = 17.5$ µm). Local nematic director field orientation is indicated with black arrows and its out-of-plane tilt, ϕ, is shown as a color map from 0° (blue) to 90° (red). C) Out-of-plane tilt of the same particle, θ_0, as a function of the cell gap, d. Optimal θ_0 is shown in green circles for 2D numerical simulations and in blue squares for experimental results. Physically impossible values of θ_0 are indicated by the red shaded region and the gray dotted-dashed indicates the point where the system becomes geometrically unrestricted (where d is greater than the diagonal size of the particle). Violet dashed line indicates the infinite cell gap asymptote of the 2D particle tilt.

becomes increasingly unlikely as L/T is increased and has not been observed experimentally in our systems.

As the cell gap is increased, we observe an increase in the optimal tilt angle of the particles, both experimentally and numerically, which are in good agreement with each other to within the experimental error range. In 2D simulations, we see that, as d is increased further, θ_0 quickly tends to an asymptote of θ_0^∞. While an analytical solution for this problem does not exist, we can describe the behavior by approximating it with a suitable function that satisfies the key criteria. First, there must exist a geometrically imposed characteristic cell gap, d_c, beyond which θ_0 changes its course and tends to θ_0^∞. Since θ_0 is guided by the blocked region, the two functions must have the same inflection point in d that is equal to $\sqrt{L^2 + T^2}$. Additionally, we can deduce that, because the function that describes the boundary of the restricted region has a nonzero gradient at $d = T$, so should θ_0. The same argument can be used to show that θ_0 must also have a nonlinear increase below d_c. This leads to the following function in the simplest form

$$\theta_0 = \left(\theta_0^\infty - \alpha\right) \tanh\left(\left(\frac{d-T}{d_c-T}\right)^2\right) + \alpha \tanh\left(\frac{d-T}{d_c-T}\right) \qquad (2)$$

where α is a constant that is responsible for the nonzero gradient at $d = T$. An example of this behavior can be seen in Figure 2C, which shows the numerical results of the optimal orientation of a particle with $L = 15$ µm, $T = 5$ µm as a function of d. Equation (2) fits this data with $\theta_0^\infty = (56.0 \pm 0.9)°$, $\alpha = (8.91 \pm 5.69)°$, and $d_c = (15.6 \pm 0.3)$ µm (equal to D_{2D}, considering the effect of the rounded corners) with an R-squared value of 0.999. By considering the balance of elastic forces arising from L and T independently from each other in the limiting case of $d \gg L, T$, we can determine that $\mathrm{atan}\sqrt{L/T}$ (equal to 60° for our particle) is close upper bound for θ_0^∞. The

actual value of θ_0^∞ is slightly less than this limit, because of the elastic distortion of the director at the corners and the outer edges of the particles (see Figure 2B). The full extent of this behavior can be visualized by considering the dimensionless version of the system using Equation (2). **Figure 3** illustrates the dependence of θ_0 as a function of the dimensionless cell gap, d/T, and the dimensionless length (i.e., the aspect ratio) of the particle, L/T. We find that these results are closely matched by our experimental observations when the inner separation gap of the parallel plate container is close to or smaller than the diagonal length of the particles. However, for systems in which d was significantly larger than L, we observed that the particles
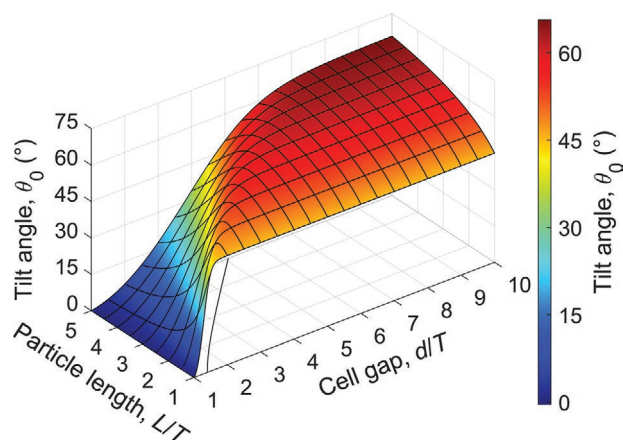

Figure 3. 2D out of plane tilt of a cuboid shaped particle in cells filled with MLC-6204-000 NLC, as a function of the dimensionless cell gap, d/T, and the dimensionless particle length, L/T. Out of plane tilt of the particle, θ_0, is shown as a color map from blue to red. The curve corresponding to the 2D diagonal length of the particle (and the end of the blocked region) is shown as a black line.

assumed a vertical configuration during the filling process of the cells with the particle–NLC solution. This is similar to the effects described in a recent study by Trebbin et al. that studied systems in which anisotropic microparticles aligned perpendicular to the flow direction in narrow microchannel.[48]

Due to the positive dielectric anisotropy of MLC-6204-000, applying an electric field across the system will begin to reorient the director to point parallel to the local voltage gradient. In turn, if $L \neq T$, this will impose an elastic torque on the particle and cause it to increase its out of plane tilt. As before, we can construct a function that closely approximates the solution by considering its key physical characteristics. Akin to the previous example, there exists a characteristic voltage, V_c, that determines the function's inflection point. However, the fact that the director has cylindrical symmetry (with **n** being physically indistinguishable from –**n**) implies that the voltage response must be described by a function that is even in V (being dielectric in nature and related to the square of the electric field) and has a θ_0 intercept with a gradient of zero. A simple function to describe this behavior is

$$\theta = (\theta_\infty - \theta_0)\left(1 - \exp\left(-\left(\frac{V}{V_c}\right)^2\right)\right) + \theta_0 \qquad (3)$$

To allow maximal reorientation capabilities, the cell gap was chosen to be sufficiently large for θ to be geometrically unrestricted but not so large that the particles stand up fully in the unperturbed state. From our experiments, we find that the cuboids ($L = W = 15$ μm, $T = 5$ μm) in $d = 17.5$ μm spaced cells are initially oriented at an angle of $(51 \pm 6)°$, which increases with increasing applied voltage and tends to an asymptote of 90° (at infinite voltage). Equation (3) fits this data with $\theta_\infty = (85.0 \pm 1.4)°$, $\theta_0 = (51.6 \pm 1.8)°$, and $V_c = (1.40 \pm 0.14)$ V with an R-squared value of 0.993. Results for this configuration are shown in **Figure 4**A,

where the experimental data is also closely matched (within the experimental error bounds) by the 2D simulations (see the Experimental Section). Individual snapshots of the 2D simulation, corresponding to a minimized free energy configuration in the L–T plane, are shown for 0 V, 1 V, and 3 V in Figure 4B.

Since the system can be described by a balance of torques on the particle, we expect that the window of angular operation must depend on L/T. This means that particles with large aspect ratios will require lower voltages to fully switch, but they will also have a lower range of possible θ. On the other hand, the particles with a lower aspect ratio will have a greater range of possible θ, but require higher voltages to achieve the same angular change. Alternatively, tangential boundary conditions on all surfaces can be used to maximize the range of electrically controllable θ in devices with $d > d_c$.

In systems where the particles are restricted from tilting beyond a certain angle by the containment geometry, there exists an additional elastic torque on the particle from the container's surfaces that opposes that of the voltage. Consequently, a higher voltage is required to change a given particle's tilt for thinner spaced cells. In **Figure 5**A we show that θ increases with increasing external voltage and reaches the asymptote that is imposed by the geometry. Equation (3) fits this data with $\theta_\infty = (30.9 \pm 1.1)°$, $\theta_0 = (20.5 \pm 2.1)°$, and $V_c = (2.31 \pm 0.70)$ V with an R-squared value of 0.857. As the voltage is increased further, θ remains unchanged. However, unlike the geometrically unrestricted case, at some point we can expect that the electric field will overpower the anchoring strength at the particle's surface and allow the defects to move around the particle. This is observed in the experimental results—once a critical voltage is reached (44 V for cuboids with $L = W = 15$ μm, $T = 5$ μm, in MLC-6204-000 filled cells with $d = 12$ μm), we observe a spontaneous change in the system. The defects break away from the corners/edges and swim toward the top and bottom faces
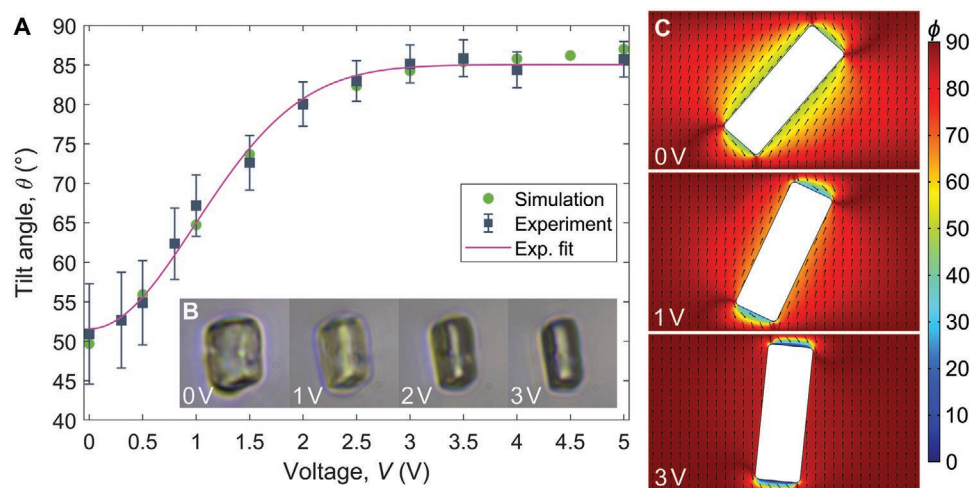

Figure 4. Experimental and numerical voltage dependence of a particle's out of plane tilt in a geometrically unrestricted cell filled with MLC-6204-000 NLC. A) Optimal tilt angle of a particle, θ, with tangential boundary conditions ($L = 15$ μm, $T = 5$ μm) in a cell ($d = 17.5$ μm) with normal boundary conditions on upper and lower cell surfaces. 2D numerical simulation results are shown in green circles, experimental results are shown in blue squares and the corresponding experimental fit using Equation (2) is show in magenta. B) Optical polarized microscopy photographs of the particle with 0, 1, 2, and 3 V applied, showing electrically driven tilt increase. C) Snapshots of the numerical simulation results at 0, 1, and 3 V that correspond to the minimal energy configuration of the particle from (A). Local nematic director field orientation is indicated with black arrows and its out-of-plane tilt of the director, ϕ, is shown as a color map from 0° (blue) to 90° (red). Voltage is applied perpendicular to the parallel plates of the cell (upper and lower surfaces in (C)).
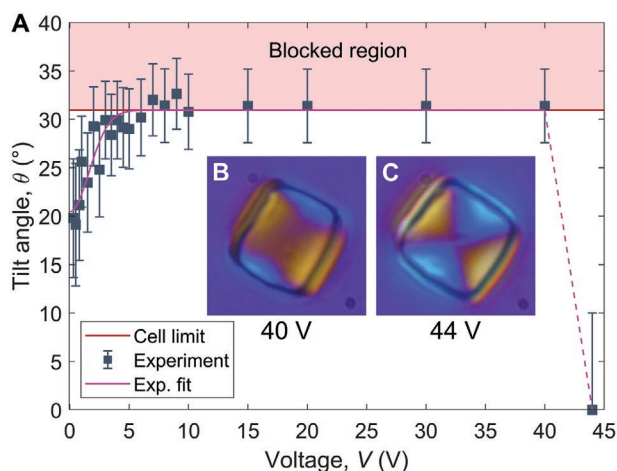
Figure 5. Experimental voltage dependence of a particle's out of plane tilt in a constricted cell filled with MLC-6204-000 nematic liquid crystal. A) Tilt angle of a cuboid shaped particle ($L = 15$ μm, $T = 5$ μm, $W = 15$ μm) in a cell ($d = 12$ μm) with normal boundary conditions on upper and lower cell surfaces. Geometrically restricted tilt angles are indicated by the shaded red region, experimental results are shown in blue squares and the corresponding fit is show in magenta. B,C) Optical polarized microscopy photographs at 40 and 44 V of the same particle, showing the transition between tilted (B) and flat (C) orientations of the particle after passing the critical voltage for defect motion. Voltage is applied perpendicular to the image plane of (B) and (C). Crossed polarizers at South-North and West-East orientations with a full wave plate inserted between them at SW–NE orientation of the slow axis.

of the particle (i.e., parallel to the $L–W$ plane). As this happens, the tilt drops suddenly to zero and the defect clearly moves to the centroid of the particle major face at 44 V, as shown in Figure 5A–C.

While the zero-tilt state shown in Figure 5B is an equilibrium state for all of the considered particles, it only becomes stable when $d < d_c$ and at high voltages. Therefore, as the voltage is removed, the defects are guided back to the opposite corners by the free energy gradients and the particle must return to a tilted state (see Figure 2C). Depending on the path that each defect takes, the particles may also experience some rotation in the $L–W$ plane. However, due to their symmetry, cuboid shaped particles tend to remain in roughly the same location and no lateral motion is induced, as shown in **Figure 6**A,C. To overcome this limitation, triangular prisms were also studied, as they are topologically equivalent to cuboids but do not have orthogonally opposing corners. When the voltage is removed and the director field relaxes, the defects move to the corners of the triangle, as shown in Figure 6B,D. The particle must move in the opposite direction to the net movement of the defects due to the relaxation of the director around the particle. The velocity of the particle decays exponentially from an initial value of (117 ± 26) μm s^{-1} with a reciprocal decay constant of (29.6 ± 2.8) ms. This results in a nonreciprocal displacement of (5.3 ± 0.8) μm over a period of (170 ± 38) ms, which closely matches the particle centroid and side of the particles' triangular faces. Following this, the particles experience a drifting motion that is partially reciprocated by the subsequent tilting of the particles as they assume an equilibrium orientation at a distance of (0.9 ± 0.3) μm from

the endpoint of the nonreciprocal displacement. An example of this is shown in **Figure 7**. Although similar nonreciprocal movement has been shown to be possible for baby skyrmion defects in bound cholesteric samples,[49] it has not been found in microparticles before.

The manifestation of nonreciprocal motion is likely due to the sequence at which each event occurs in the system. When the particle is in the high tilt state, but the voltage is insufficient to break the surface anchoring of the defects, it is in close proximity to the boundaries of the cell (see Figures 5A and 7B). Since viscous forces are more prominent closer to the boundaries, the defects move through the reorientation of the director and the particles can only rotate when the critical voltage is applied, leaving little energy for translation. On the other hand, when the particle is in the low tilt state, it is far away from the walls of the container and translational motion is easier, as shown in Figure 7F.

Sudden removal of voltage leads to a much slower relaxation of the director and the decoupling between director reorientation and flow is lost. This allows the particle to swim first and rotate back to equilibrium later. This means that an on–off sequence of voltages (above the critical value) can be used to create discretized net motion of the particles in a particular direction.

Considering the symmetry of the particles, we deduce that translational motion should only occur in particles (assuming homogeneous thickness) with an odd number of corners on their shape defining faces (e.g., platelets formed from triangular, pentangular or heptangular faces with smaller, rectangular sided walls). Moreover, as the number of corners is increased, the maximal distance of translational motion is decreased. Since the defects are guided by the elastic free energy gradients to be as far from each other as possible, equilateral triangular prisms have the largest potential for translational motion. This can be emphasized using hyperbolic triangles, as they will have more prominent minimal energy paths for the defects to travel along. Furthermore, we can expect that the direction of motion can be controlled by using hyperbolic triangular prisms with two of the corners being sharper than the rest to act as designated docking stations for the defects. In addition to the differences in shape, local variation of the surface anchoring should allow increased controled of electrophoresis for these particles.

3. Conclusions

In conclusion, we have investigated the effects of geometric symmetry on electrically induced quasi-static and dynamic reorientation and motion of particles with tangential boundary conditions in NLCs. By considering the balance of torques, we have shown that these particles tilt at an angle that depends on the aspect ratio of the particles and their relative size to the cells containing them. Furthermore, the tilt angle can be controlled by applying an external electric field, through which the particles can assume a fully standing position in geometrically unrestricted systems. Similar behavior is found in geometrically restricted systems. In this case, it is physically impossible for the particles to tilt beyond a certain
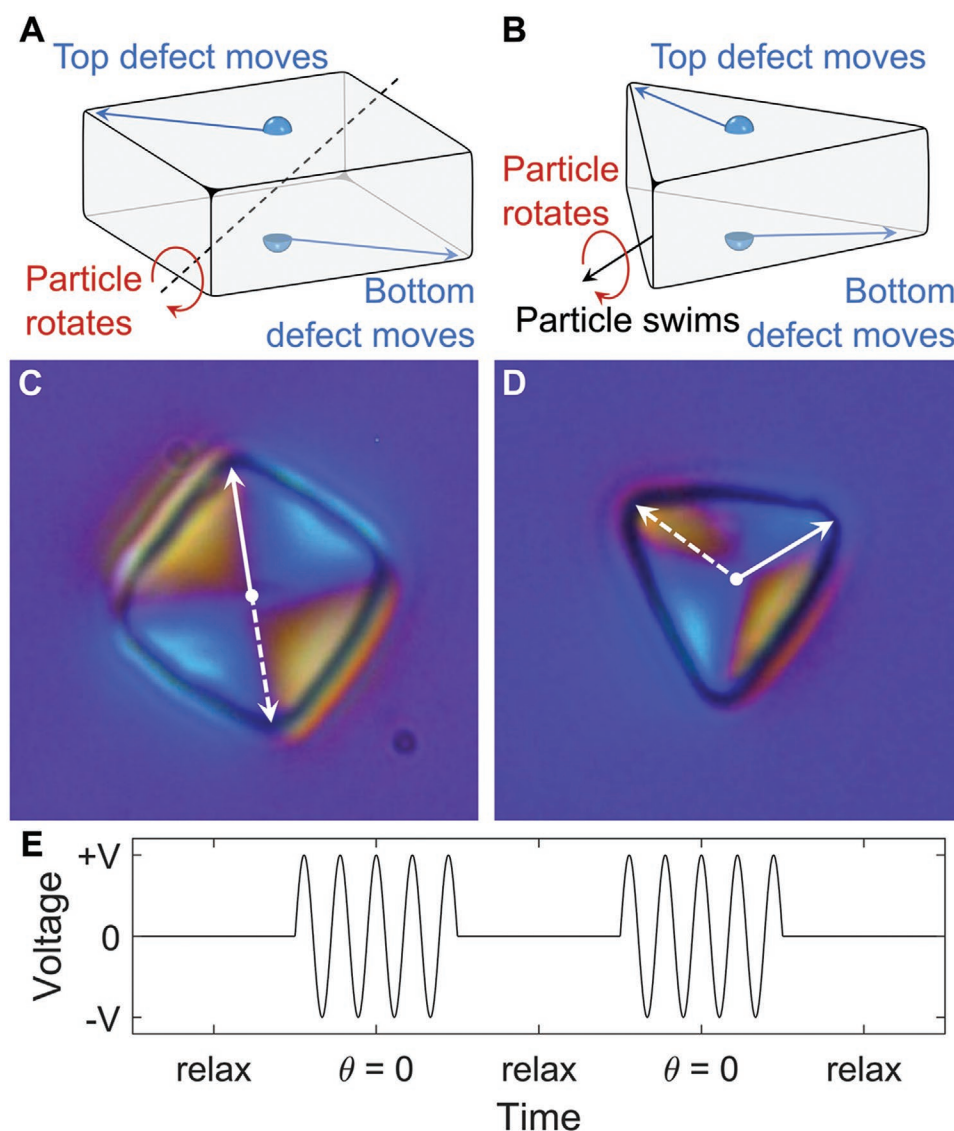
Figure 6. Dynamics of microparticles caused by the motion of topological defects after the removal of high voltage. A,B) Schematic diagrams illustrating the motion of topological defects toward opposing corners of the top and bottom faces of a cuboid and a triangular prism shaped particles and the subsequent dynamics of the particles after the removal of an external voltage sufficiently high to cause anchoring breaking and particle reorientation to the horizontal condition. Due to the direction of motion of the defects in each case, cuboids rotate along the axis that is perpendicular to the plane of motion of its topological defects. On the other hand, the net direction of defects' motion causes the triangles to swim in the opposite direction. C,D) Optical polarized microscopy photographs of a cuboid ($L = 15$ μm, $T = 5$ μm, $W = 15$ μm) and a triangular prism (side length = 15 μm, $T = 5$ μm) shaped particles at 44 V in a cell with $d = 12$ μm. Motion of the topological defects is indicated by the arrow directions. Crossed polarizers at South-North and West-East orientations with a full wave plate inserted between them at SW–NE orientation of the slow axis. E) Typical voltage sequence that was used to produce nonreciprocal motion (frequency of the oscillating voltage is exaggerated for illustration purposes).

angle and increasing the voltage past a critical value breaks the surface anchoring and allows the defects to relocate to the centers of the top and bottom faces of the particles. Removing the high voltage causes the defects to travel to the opposite corners of the particle, which allows it to resume a high tilt state. We observe that geometry plays a key role in the subsequent motion of the particles. By symmetry, the centroids of the cuboid shaped particles remain stationary during this process while the triangular particles are able to move in a direction that is perpendicular to that of the applied electric

field. In fact, this process is nonreciprocal and the triangular prisms are able to travel forward in a stop-motion-like fashion when an on–off sequence of high voltages is applied across the sample. These findings are beginning to show how both rotation and translation of particles can be controlled through the shape of the particle and its containment. Work is underway on providing different properties to the particle faces (including reflectance, fluorescence, absorption, and alignment) to produce a variety of functional particles controlled through the application of electric fields.
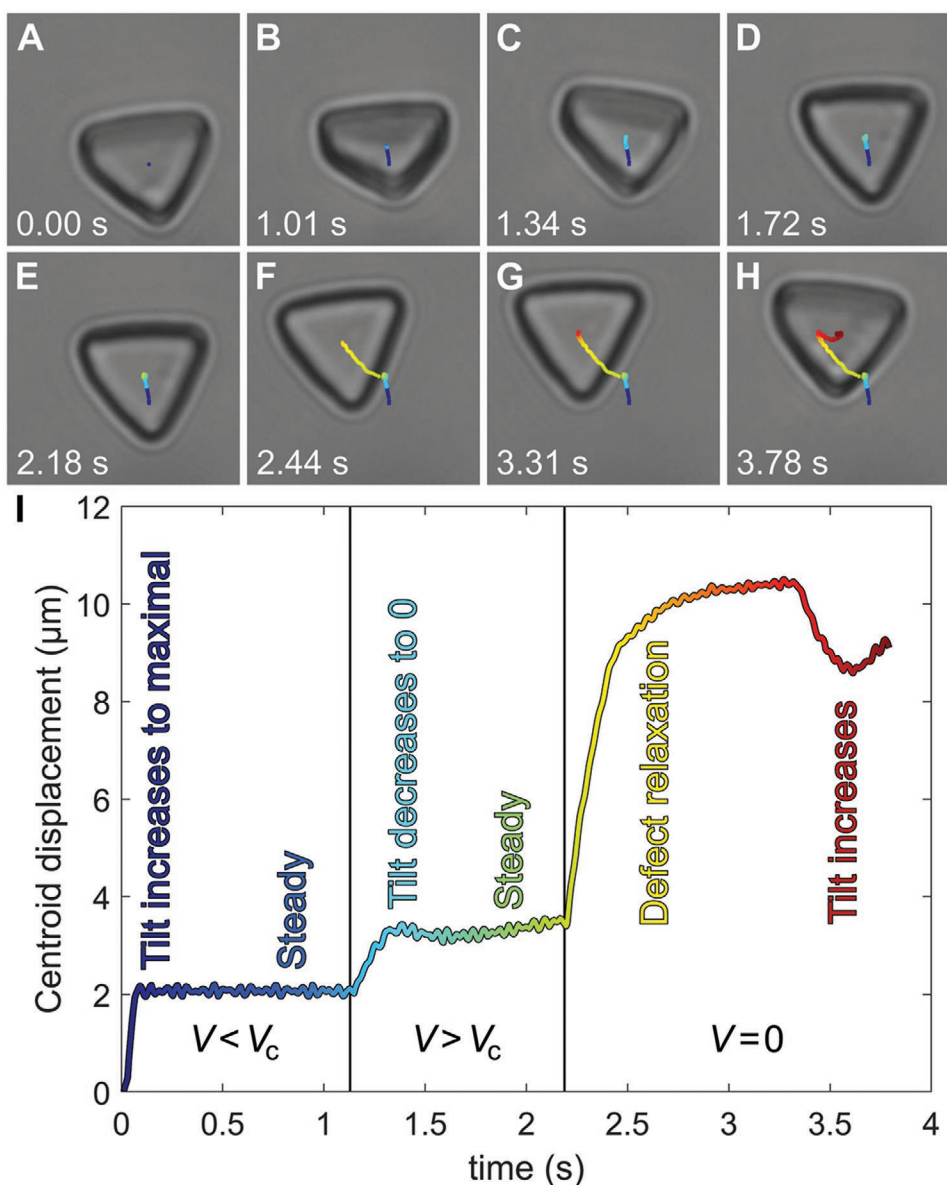
ADVANCED
SCIENCE NEWS
www.advancedsciencenews.com

NANO · MICRO
small
www.small-journal.com

Figure 7. Image sequence showing positional tracking of a triangular prism with (side length = 15 μm, T = 5 μm), contained within a cell of gap d = 12 μm. Path line represents the positioning of the centroid as a color coded function of time (see Video S1, Supporting Information) A) No external voltage is applied. B) Particle tilt increases when external voltage (below the critical value) is applied. C) Increasing voltage beyond the critical value induces reorientation of the particle. D) Highest symmetry axis of the particle fully aligns with the average electric field direction. E) Voltage is removed. F) Symmetric director configuration becomes unstable and the particle is laterally transposed. G) Particle drifts further at a much slower velocity. H) Particle partially reciprocates the drifting motion and tilts out of plane to assume an equilibrium state. I) Relative position of triangular prism centroid with applied field.

4. Experimental Section

Microparticle Fabrication: To achieve a particle thickness of 5 μm, SU-8 2025 negative photoresist (MicroChem Corp.) was diluted in cyclopentanone at a 35% concentration (w.r.t. mass) and spin-coated onto a clean glass slide for 10 s at 500 rpm, followed by 30 s at 3000 rpm. The film was then soft baked for 60 s at 65 °C, followed by 60 s at 95 °C. Following this, the particles were drawn into the substrate by exposing a predetermined set of coordinates of the film to a 375 nm light source using the Microwriter ML2 Direct Write Laser system (Durham Magneto Optics). The substrate was then baked for 60 s at 95 °C and developed in 1-methoxy-propyl acetate to dissolve the unexposed regions of the photoresist. The substrate was cleaned with 2-propanol and hard baked for 10 min at 140 °C. The particles were dislodged from the substrate

and mixed with a drop of MLC-6204-000 at 80 °C (above the nematic-to-isotropic phase transition temperature) with a resulting concentration of (1.5 ± 0.5) particles per nanoliter.

Device Fabrication: Indium tin oxide (ITO) glass slides (sheet resistance of 15 Ω sq⁻¹) were cleaned using 5%, 0.5%, and 0% solutions of Decon 90 detergent (Decon Laboratories) in deionized water and ultrasonicated for 15 min at 60 °C each, while thoroughly rinsing with deionized water between steps. The substrates were then soaked in 2-propanol, blow dried, and treated with UV-ozone for 30 min. Following this, SE1211 was diluted in dimethylformamide at a 66% concentration (w.r.t. mass), spin-coated onto the clean ITO glass slides for 10 s at 500 rpm and 30 s at 3000 rpm, and baked for 120 min at 180 °C. The parallel plate capacitor cells were constructed using Mylar spacer films of various thicknesses to control the inner separation gaps and sealed

with UV-sensitive glue on two opposite sides. The inner separation gaps of each device were measured using interference spectrometry to be (12.0 ± 0.5) µm, (16.0 ± 0.5) µm, (17.5 ± 0.5) µm, (23.0 ± 0.5) µm, and (35.0 ± 0.5) µm. Finally, the devices were filled with the particle–NLC mixture at 80 °C using capillary forces and sealed around their perimeters, while still allowing room for electrical connections.

Microscopy and Electrical Addressing: Devices were studied using a Leica DM2700P cross-polarizing microscope with a ×50 objective and imaged using an EO-23121C camera (Edmund Optics). Electrical addressing was performed by applying 10 kHz sine waves with increasing voltages using a 33622A (Keysight Technologies) arbitrary waveform generator across the samples. For the case of dynamic motion, an additional 0.5 Hz pulse envelope wave was used to switch between the on and off states. The voltage was monitored using a TDS2014 (Tektronix Inc.) oscilloscope and a 34419A (Keysight Technologies) digital voltmeter.

Numerical Methods: Simulations of the nematic order tensor, $Q_{ij} = Q(n_i n_j - \delta_{ij}/3)$, were performed using commercial finite element analysis software (COMSOL 5.4a) through the minimization of the Landau–de Gennes free energy

$$U = \int_\nu u_\nu \mathrm{d}\nu + \int_s u_s \mathrm{d}s \tag{4}$$

where u_ν is the bulk free energy density term and u_s is a boundary term that determines the director's orientation at the corresponding surface. Under the single elastic constant approximation, the following equation is set

$$u_\nu = a Q_{ij} Q_{ij} + \frac{2b}{3} Q_{ij} Q_{jk} Q_{ki} + \frac{c}{2}\left(Q_{ij} Q_{ij}\right)^2 + \frac{L_1}{2}\left(\frac{\partial Q_{ij}}{\partial x_k}\right)^2 - \frac{1}{2}\varepsilon_0 \varepsilon_{ij} \frac{\partial V}{\partial x_i}\frac{\partial V}{\partial x_j} \tag{5}$$

where a, b, and c are the critical thermal coefficients, L_1 is the elastic constant, ε_0 is the permittivity of free space, ε_{ij} is the relative permittivity tensor (with an eigenvalue set $\{\varepsilon_1, \varepsilon_2, \varepsilon_3\}$ in the reference frame of the director), and V is the voltage. In the calculations, the values are set as $a = -162$ kJ m^{-3}, $b = -270$ kJ m^{-3}, $c = 900$ kJ m^{-3}, $L_1 = 12$ pN, $\varepsilon_1 = \varepsilon_2 = \varepsilon_3 = 3.8$ for the electrically isotropic particles and $\varepsilon_1 = \varepsilon_2 = 8.84$, $\varepsilon_3 = 38.1$ for the anisotropic NLC. These values correspond to an equilibrium NLC order parameter $Q = (-b + \sqrt{b^2 - 24ac})/4c$ of 0.6 and a nematic correlation length of 4 nm. The electric field is calculated self consistently with both the director field and the particle orientation. To model degenerate tangential BCs on the particles, the following equation is used

$$u_s = W_s\left(\left(\tilde{Q}_{ij} - \tilde{Q}_{ij}^\perp\right)^2 + \left(\tilde{Q}_{ij}^2 - Q^2\right)^2\right) \tag{6}$$

where $\tilde{Q}_{ij} = Q_{ij} + \frac{Q}{3}\delta_{ij}$, $\tilde{Q}_{ij}^\perp = (\delta_{ik} - m_i m_k)\tilde{Q}_{kl}(\delta_{lj} - m_l m_j)$, **m** is the outward pointing unit normal to the surface s, and W_s is the anchoring strength of the director on the surface s.[50] Strong anchoring conditions were achieved by setting $W_s = 1$ cJ m^{-2}.

Optimal configurations of the particles were found by evaluating U across a range of particle tilt angles and locating the points at which it was minimized. This procedure was repeated for different values of d and V.

Data Availability

All data are available from the corresponding author on reasonable request.

Supporting Information

Supporting Information is available from the Wiley Online Library or from the author.

Conflict of Interest

The authors declare no conflict of interest.

Author Contributions

N.V.S. and A.S. contributed equally to this work. N.V.S., A.S., and J.C.J. designed the research. A.S. performed the experiments and N.V.S. performed the analysis and numerical simulations, both under the supervision of J.C.J.. J.C.J., N.V.S., and A.S. wrote this paper.

[1] V. N. Manoharan, *Science* **2015**, *349*, 1253751.
[2] W. J. Parak, D. Gerion, T. Pellegrino, D. Zanchet, C. Micheel, S. C. Williams, R. Boudreau, M. A. L. Gros, C. A. Larabell, A. Alivisatos, *Nanotechnology* **2003**, *14*, R15.
[3] J. R. Lakowicz, *Plasmonics* **2006**, *1*, 5.
[4] F. Li, D. Josephson, A. Stein, *Angew. Chem., Int. Ed.* **2011**, *50*, 360.
[5] F. Zhang, H. Zhong, C. Chen, X.-g. Wu, X. Hu, H. Huang, J. Han, B. Zou, Y. Dong, *ACS Nano* **2015**, *9*, 4533.
[6] H. Huang, L. Polavarapu, J. A. Sichert, A. S. Susha, A. S. Urban, A. L. Rogach, *NPG Asia Mater.* **2016**, *8*, e328.
[7] B. Comiskey, J. D. Albert, H. Yoshizawa, J. Jacobson, *Nature* **1998**, *394*, 253.
[8] I. C. Sage, *US Patent No. 7394509*, **2008**.
[9] Y. Fang, M. Sun, *Light: Sci. Appl.* **2015**, *4*, e294.
[10] S. A. Maier, G. Kik, H. A. Atwater, S. Meltzer, E. Harel, B. E. Koel, A. A. Requicha, *Nat. Mater.* **2003**, *2*, 229.
[11] M. Quinten, A. Leitner, J. R. Krenn, F. R. Aussenegg, *Opt. Lett.* **1998**, *23*, 1331.
[12] S. Sivakumar, K. L. Wark, J. K. Gupta, N. L. Abbott, F. Caruso, *Adv. Funct. Mater.* **2009**, *19*, 2260.
[13] P. Bao, D. A. Paterson, P. L. Harrison, K. Miller, S. Peyman, J. C. Jones, J. Sandoe, S. D. Evans, R. J. Bushby, H. F. Gleeson, *Lab Chip* **2019**, *19*, 1082.
[14] C. Lapointe, S. Hopkins, T. G. Mason, I. I. Smalyukh, *Phys. Rev. Lett.* **2010**, *105*, 178301.
[15] U. Tkalec, M. Ravnik, S. Čopar, S. Žumer, I. Muševič, *Science* **2011**, *333*, 62.
[16] A. Nych, U. Ognysta, M. Škarabot, M. Ravnik, S. Žumer, I. Muševič, *Nat. Commun.* **2013**, *4*, 1489.
[17] Q. Liu, B. Senyuk, M. Tasinkevych, I. I. Smalyukh, *Proc. Natl. Acad. Sci. USA* **2013**, *110*, 9231.
[18] O. D. Lavrentovich, *Soft Matter* **2014**, *10*, 1264.
[19] D. A. Beller, M. A. Gharbi, I. B. Liu, *Soft Matter* **2015**, *11*, 1078.
[20] Q. Liu, P. J. Ackerman, T. C. Lubensky, I. I. Smalyukh, *Proc. Natl. Acad. Sci. USA* **2016**, *113*, 10479.

[21] Y. Yuan, A. Martinez, B. Senyuk, M. Tasinkevych, I. I. Smalyukh, *Nat. Mater.* **2018**, *17*, 71.

[22] Y. Yuan, G. N. Abuhaimed, Q. Liu, I. I. Smalyukh, *Nat. Commun.* **2018**, *9*, 5040.

[23] N. V. Solodkov, J.-U. Shim, J. C. Jones, *Nat. Commun.* **2019**, *10*, 198.

[24] P. G. de Gennes, J. Prost, *The Physics of Liquid Crystals. International Series of Monographs on Physics*, Clarendon Press, Oxford **1993**.

[25] L. M. Blinov, *Structure and Properties of Liquid Crystals*, Springer Science & Business Media, Heidelberg **2011**.

[26] F. C. Frank, *Discuss. Faraday Soc.* **1958**, *25*, 19.

[27] Ž. Kos, J. Aplinc, U. Mur, M. Ravnik, *Flowing Matter* (Eds: F. Toschi, M. Sega), Springer International Publishing, Cham **2019**, pp. 51–93.

[28] N. D. Mermin, *Rev. Mod. Phys.* **1979**, *51*, 591.

[29] M. Kleman, O. D. Lavrentovich, *Philos. Mag.* **2006**, *86*, 4117.

[30] H. Stark, *Phys. Rep.* **2001**, *351*, 387.

[31] G. Alexander, B. G.-G. Chen, E. A. Matsumoto, R. D. Kamien, *Rev. Mod. Phys.* **2012**, *84*, 497.

[32] W. P. Thurston, *Three-Dimensional Geometry and Topology*, Vol. *1*, Princeton University Press, NJ **1997**.

[33] N. Schopohl, T. J. Sluckin, *Phys. Rev. Lett.* **1987**, *59*, 2582.

[34] G. P. Bryan-Brown, C. V. Brown, J. C. Jones, E. L. Wood, I. C. Sage, P. Brett, J. Rudin, *SID Int. Symposium Dig. Tech. Pap.* **1997**, *28*, 37.

[35] J. C. Jones, *J. Soc. Inf. Disp.* **2008**, *16*, 143.

[36] I. Muševič, M. Škarabot, U. Tkalec, M. Ravnik, S. Žumer, *Science* **2006**, *313*, 954.

[37] M. Ravnik, S. Žumer, *Soft Matter* **2009**, *5*, 4520.

[38] J.-K. Guo, S.-H. Hong, H.-J. Yoon, G. Babakhanova, O. D. Lavrentovich, J. K. Song, *Adv. Sci.* **2019**, *6*, 1900785.

[39] I. Abdulhalim, P. Lakshmi Madhuri, M. Diab, T. Mokari, *Opt. Express* **2019**, *27*, 17387.

[40] P. Lakshmi Madhuri, R. J. Martin-Palma, B. Martín-Adrados, I. Abdulhalim, *J. Mol. Liq.* **2019**, *281*, 108.

[41] C. Lapointe, A. Hultgren, D. M. Silevitch, E. J. Felton, D. H. Reich, R. L. Leheny, *Science* **2004**, *303*, 652.

[42] C. Lapointe, T. G. Mason, I. I. Smalyukh, *Science* **2009**, *326*, 1083.

[43] Y. Luo, D. A. Beller, G. Boniello, F. Serra, K. J. Stebe, *Nat. Commun.* **2018**, *9*, 3841.

[44] A. del Campo, C. Greiner, *J. Micromech. Microeng.* **2007**, *17*, R81.

[45] M. Ravnik, S. Žumer, *Liq. Cryst.* **2009**, *36*, 1201.

[46] A. M. Sonnet, E. G. Virga, *Dissipative Ordered Fluids: Theories for Liquid Crystals*, Springer Science & Business Media, New York **2012**.

[47] N. J. Mottram, C. J. Newton, arXiv:1409.3542 **2014**.

[48] M. Trebbin, D. Steinhauser, J. Perlich, A. Buffet, S. V. Roth, W. Zimmermann, J. Thiele, S. Förster, *Proc. Natl. Acad. Sci. USA* **2013**, *110*, 6706.

[49] P. J. Ackerman, T. Boyle, I. I. Smalyukh, *Nat. Commun.* **2017**, *8*, 673.

[50] J.-B. Fournier, P. Galatola, *Europhys. Lett.* **2005**, *72*, 403.